



An efficient neural network based method for medical image segmentation



Nima Torbati, Ahmad Ayatollahi*, Ali Kermani

Department of Electrical Engineering, Iran University of Science and Technology, Tehran, Iran

ARTICLE INFO

Article history:

Received 3 January 2013

Accepted 31 October 2013

Keywords:

Artificial neural network (ANN)

Medical image segmentation

Computer aided diagnosis (CAD) systems

Pattern recognition

ABSTRACT

The aim of this research is to propose a new neural network based method for medical image segmentation. Firstly, a modified self-organizing map (SOM) network, named moving average SOM (MA-SOM), is utilized to segment medical images. After the initial segmentation stage, a merging process is designed to connect the objects of a joint cluster together. A two-dimensional (2D) discrete wavelet transform (DWT) is used to build the input feature space of the network. The experimental results show that MA-SOM is robust to noise and it determines the input image pattern properly. The segmentation results of breast ultrasound images (BUS) demonstrate that there is a significant correlation between the tumor region selected by a physician and the tumor region segmented by our proposed method. In addition, the proposed method segments X-ray computerized tomography (CT) and magnetic resonance (MR) head images much better than the incremental supervised neural network (ISNN) and SOM-based methods.

© 2013 Elsevier Ltd. All rights reserved.

1. Introduction

Medical image analysis plays a key role in computer aided diagnosis (CAD) systems. It involves fundamental steps like enhancement, segmentation, registration and visualization, among which segmentation which divides an image into its constructed regions is the first step in many medical image analyses [1]. Medical images are often corrupted by noise due to several reasons. The first one is that different imaging modalities use different acquisition techniques; secondly, during the acquisition the image is formed under the influence of different physical phenomena and finally, specific technical limitations that accompanies each imaging modality. Several methods such as edge detection, thresholding, region growing, clustering and artificial neural networks (ANN) have been proposed for segmenting medical images. Edge detectors, like canny [2], are not suitable for segmenting medical images. One reason is that medical images are usually corrupted by noise. However, edge detectors determine edges with the local information in the neighborhood of a pixel. Therefore, real edges are never formed in medical images [3]. So, pre-processing steps are needed to reduce the noise effect.

Intensity distribution in medical images is so complex that makes it difficult to determine the threshold value. Thus thresholding

methods on their own are not suitable, and they have to be combined with other methods [4].

By using predetermined similarity criteria, region growing methods gather pixels or sub-regions from larger regions. Successful methods such as those proposed in [5,6] suffer from sensitivity to the selection of initial seed points.

Clustering is a popular method for medical image segmentation. Among clustering techniques, the fuzzy c-mean (FCM) [8] has received much attention since it preserves more information from the original image compared to other segmentation methods [7,9,10].

Artificial neural network (ANN) has been widely used in medical image analysis fields such as segmentation, data compression, image enhancement and noise suppression [11,12]. Multi-layer perceptron (MLP), self-organizing maps (SOM), Hopfield and pulse coupled neural networks have been also utilized for medical image segmentation [13–18,29,30]. SOM network is one of the most suitable networks used for segmentation. This is an unsupervised network based on the competitive learning and discovering topological structure hidden in the input data for visual display in one or two dimensional spaces [19]. Two great advantages of the SOM based segmentation methods are unsupervised training and fast learning. There are some disadvantages to segmentation methods which use this network. The first drawback is that increasing the number of neurons in this network does not usually result in a better segmentation performance. The second disadvantage is that they need high dimensional input space with empirical features for an optimal performance [20]. And finally that they cannot segment images with heavy noise successfully.

* Corresponding author. Tel.: +98 912 137 4823.

E-mail address: ayatollahi@iust.ac.ir (A. Ayatollahi).

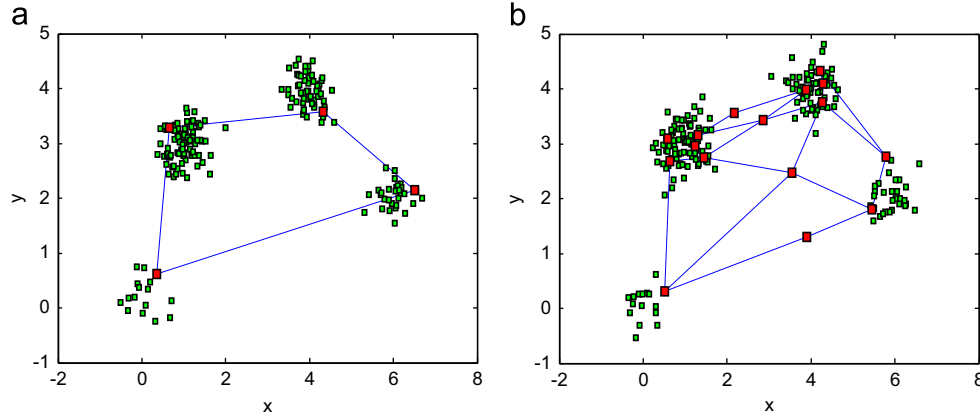


Fig. 1. (a) Classification result of the 2×2 SOM network. (b) Classification result of the 4×4 SOM network. (For interpretation of the references to color in this figure, the reader is referred to the web version of this article.)

To overcome the first problem of SOM networks, an incremental method has been proposed in [15]. But, in fact, increasing the number of neurons in the first layer of a SOM network does not decrease the segmentation accuracy. This comes from the concept of SOM network as shown in Fig. 1. This figure shows a two-dimensional (2D) feature space with four classes. The red quadrangles denote neurons and the blue lines show the interconnections between the neurons. The feature space is classified by 2×2 and 4×4 SOM networks in Fig. 1(a) and (b), respectively. Both networks have classified the space properly, however neurons in Fig. 1(b) display the topological structure of the input better than the neurons in Fig. 1(a). As can be observed, the dense classes have more neurons. Therefore, increasing the number of neurons in a SOM network results in an enhanced classification. But considering Fig. 1(b), if the neuron lying in a specific cluster does not join other neurons in that cluster, the samples near that neuron are incorrectly classified as extra clusters. As a result, the problem of the SOM is not the initial selection of the number of neurons but merging these neurons properly. In other words, after the segmentation is done, a post-processing step is required to unite the neurons belonging to a specific cluster.

Tucci et al. proposed a new structure for SOM networks based on a new neuron model [21]. In this network called FIR-SOM, each neuron acts as a finite impulse response (FIR) system. In a trained FIR-SOM network with constant filter coefficients, neurons of the first layer present a moving average (MA) filter regardless of the underlying input distribution. This property makes the network more robust against noise and sparse samples in the input space.

In order to rectify the drawbacks of segmentation methods based on the SOM network, we propose a merging MA-SOM (MMA-SOM) method for segmenting two dimensional medical images. The proposed method utilizes MA-SOM network to segment medical images. After that, a merging process is initiated to connect the objects of a joint cluster together. Then a two dimensional (2D) discrete wavelet transform (DWT) is used to build the input feature space of the network. The experimental results show that MA-SOM discovers the pattern of the input image properly, and is robust against noise. The segmentation results of breast ultrasound images (BUS) demonstrate that there is a significant correlation between the tumor region selected by a physician and the tumor region segmented by our proposed method. In addition, the proposed method segments X-ray computerized tomography (CT) and magnetic resonance (MR) head images much better than the incremental supervised neural network (ISNN) [20] and SOM network based methods.

The rest of the paper is organized as follows: Section 2 describes FIR-SOM networks and introduces the proposed

method; Section 3 presents the experimental results, and the two last sections discuss the concluding remarks of the paper.

2. The proposed MMA-SOM segmentation algorithm

Each neuron in a FIR-SOM network is defined as a FIR system of order M . The weight vector $\omega(t)$ is shown by the linear combination of the last M values of input $x(t)$ as

$$\omega(t) = \sum_{k=1}^M a_k(t)x(t-k), \quad (1)$$

where $[a_1(t), a_2(t), \dots, a_M(t)]$ are the samples of the impulse response of the system and $t = 1, 2, \dots$ represents the time steps.

In SOM networks, all neurons receive the same input sample $x(t)$ at any training step. However, in FIR-SOM networks, each neuron receives a personalized input sequence that is influenced by its neighbors' cooperation. Therefore, in order to obtain the trace of the last M values of the input $x(t)$ to the neuron i , each neuron is associated with a set of M trace vectors $[x_i(t-1), x_i(t-2), \dots, x_i(t-M)]$. These vectors build the following trace matrix:

$$X_i(t) = [x_i^1(t), x_i^2(t), \dots, x_i^M(t)]. \quad (2)$$

In this FIR system, the trace and weight vectors represent the input and output, respectively. Thus, if the columns of the trace matrix $X_i(t)$ represent the sequence of the last M inputs to neuron i , the weight vector ω_i of the neuron can be shown as

$$\omega_i(t) = \sum_{k=1}^M a_i^k(t)x_i^k(t) = X_i(t)a_i(t), \quad (3)$$

where each neuron i has its own set of FIR coefficients $[a_i^1(t), a_i^2(t), \dots, a_i^M(t)]$. At each training step, it is necessary to perform a single step time shift of the trace vectors. This is obtained by a shift of the trace matrix $X_i(t)$ as follows:

$$X_i^{t+1} = [x(t), x_i^1(t), \dots, x_i^{M-1}(t)], \quad (4)$$

where \hat{X}_i^{t+1} represents the trace matrix after a single step time shift of the trace vectors. At each training step, the trace matrix is updated by the following equation:

$$X_i(t+1) = X_i(t) + \eta_{ci}(t)(\hat{X}_i^{t+1} - X_i(t)), \quad (5)$$

where c is the winning neuron; and $\eta_{ci}(t)$ is a neighborhood function:

$$\eta_{ci}(t) = \exp\left(\frac{-d^2(c, i)}{2\sigma^2(t)}\right) \quad (6)$$

where $d(c, i)$ is the distance metric between the two neurons c and i ; and σ is the effective width of the neighborhood function. By using (5), the trace vectors of the winning neuron and its topological neighbors are updated. However, the trace vectors of the neurons that are far from the winner neuron will remain approximately unchanged.

In case that the filter coefficients are constant, i.e. $a_i^k = 1/M$, the FIR system is a MA one and the updated equation of the weight vectors can be obtained by substituting (5) in (3) as follows:

$$\omega_i(t+1) = X_i(t+1)a_i = \omega_i(t) + \eta_{ci}(t)(\hat{\omega}_i^{t+1} - \omega_i(t)), \quad (7)$$

where

$$\hat{\omega}_i^{t+1} = \hat{X}_i^{t+1}a_i = \frac{1}{M}(x(t) + \sum_{k=2}^M x_i^{k-1}(t)). \quad (8)$$

It is easy to realize from (7) that the weight vector $\omega_i(t)$ moves toward the filter output vector $\hat{\omega}_i^{t+1}$ which represents the target value in (7). While, in the classic SOM, the target value is represented by input vector $x(t)$ [21].

The rest of this section describes in more detail how the proposed MMA-SOM algorithm segments medical images. The flow chart of our method is shown in Fig. 2.

In this study, we use a MA-SOM network with three input nodes (equal to feature dimension) in the input layer and a 2D lattice in the first layer. A 2D structure for the first layer is used because it preserves the topological property better than a 1D one. The proposed method is described in the following four steps:

Step I: Feature extraction

A 2D-DWT is applied to the input image for two different scale parameters to build two filtered images. Both detail and general features of the input image can be analyzed by using the 2D-DWT [1]. Scale parameter plays an important role in the 2D-DWT. When this value increases (resp. decreases), low (resp. high) frequency band components of image appear.

In this method, a 2D-DWT of the whole image with a scale parameters of 1 and 2 is computed. For each pixel, the intensity of these two filtered images and the original one form the 3D input feature space for the MA-SOM network.

Step II: Network training

Similar to many networks, the MA-SOM network also needs an initial setup described in the following:

The first initial setup: The number of neurons at the first layer can be manually chosen with regard to the number of objects in the image determined by an expert physician, K . Then, we select first $N \times N$ network which contains more neurons for the network structure than K since we believe that the merging process will connect the adjacent neurons.

The second initial condition: Increasing the number of trace vectors associated with each neuron can lead to a better segmentation performance. However, this increment can no

longer affect the performance as it reaches to a specific steady value [21,22]. In the proposed segmentation method, both proper performance and the low number of multiplications can be achieved when the number of trace vectors is considered equal to 5. It should be mentioned that this value has been experimentally determined after more than 1000 trials.

The initial values of trace vectors, weight vectors and training set are drawn randomly from the input image. Afterward, Eqs. (5) and (7) are utilized to update the weight and the trace vectors.

Step III: Segmentation

For segmenting the input image into different objects, the whole image is fed into the trained network pixel by pixel. For the feature vector of each pixel, based on the Euclidean minimum distance criterion, there is a winner neuron in the first layer which specifies the corresponding object with a pixel.

Step IV: Merging process

As described in Section 1, in order to restrain misclassification, a process is needed after the segmentation to connect neurons which belong to a common class. In order to join these neurons, we should recognize the existing clusters in the network structure, for the purpose of which the following method is used:

2.1. Cluster recognition

The threshold vector T is defined as

$$T = (t_i)_{1 \times Z}, \quad i = 1, \dots, Z \\ t_i = T_0 + i\Delta t, \quad (9)$$

where T_0 is an initial threshold value; Z is a positive number indicating the threshold range, and Δt is a step value denoting the threshold accuracy. For each t_i , we compose a neighborhood matrix B which has the same size as that of the neurons' structure in the first layer:

$$B = [b_{f,g}]_{F \times G}, \quad (10)$$

where each $b_{f,g}$ has a binary value that shows the nearness of neurons f and g . Then, the Euclidean distance between the weight vectors of neuron f and g is computed. If this distance is greater than t_i , the value of $b_{f,g}$ is one, otherwise, it is zero. In other words,

$$b_{ij} = \begin{cases} 1 & \text{if } d(f,g) \leq T \\ 0 & \text{otherwise} \end{cases} \quad (11)$$

where $d(f,g)$ is the Euclidean distance between the weight vectors of neuron f and g .

After the formation of the neighborhood matrix, the row with most ones (v)—that is corresponding to the neuron with most neighbors—is selected:

$$v = \arg \max_f \left\{ \sum_{g=1}^G b_{f,g} \right\} \quad (12)$$

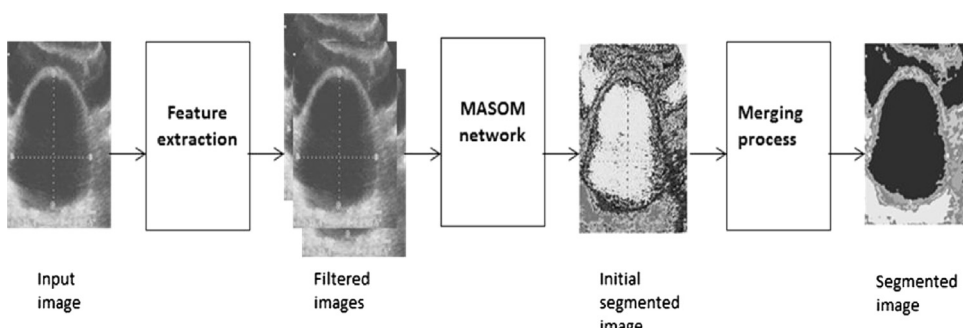


Fig. 2. Flow chart of the proposed method.

This neuron and its neighbors shape a cluster (c) for which we define the volume value (S_c) as

$$S_c = (Z(m_c)X(d(\nu, l)))^N \quad (13)$$

where m_c is the number of neurons in the cluster; N is the dimension of the feature space, and l is a neuron which belongs to this cluster. In the case of medical images, we have used the following volume value:

$$S_c = \left(\frac{1}{m_c} \sum_{l=1}^{m_c} d(v, l) \right)^N, \quad (14)$$

Then, this cluster and its neurons are removed from the network, and for the same value of t_i , the merging process starts

again from (10) with the remaining neurons. This progress continues until all clusters in the network are recognized.

2.2. Threshold selection

After recognizing clusters in the neurons' structure corresponding to each t_i , the best threshold value for them is computed by

$$T_{best} = \arg \max_i D_{t_i} \quad \forall t_i \in T, i = 1, \dots, Z \quad (15)$$

In (15), T_{best} is the best threshold value and D_{t_i} is computed by

$$D_{t_i} = \frac{1}{C} \sum_{c=1}^C \frac{m_c^\lambda}{S_c^{\eta}} \quad \forall t_i \in T, i = 1, \dots, Z, \quad (16)$$

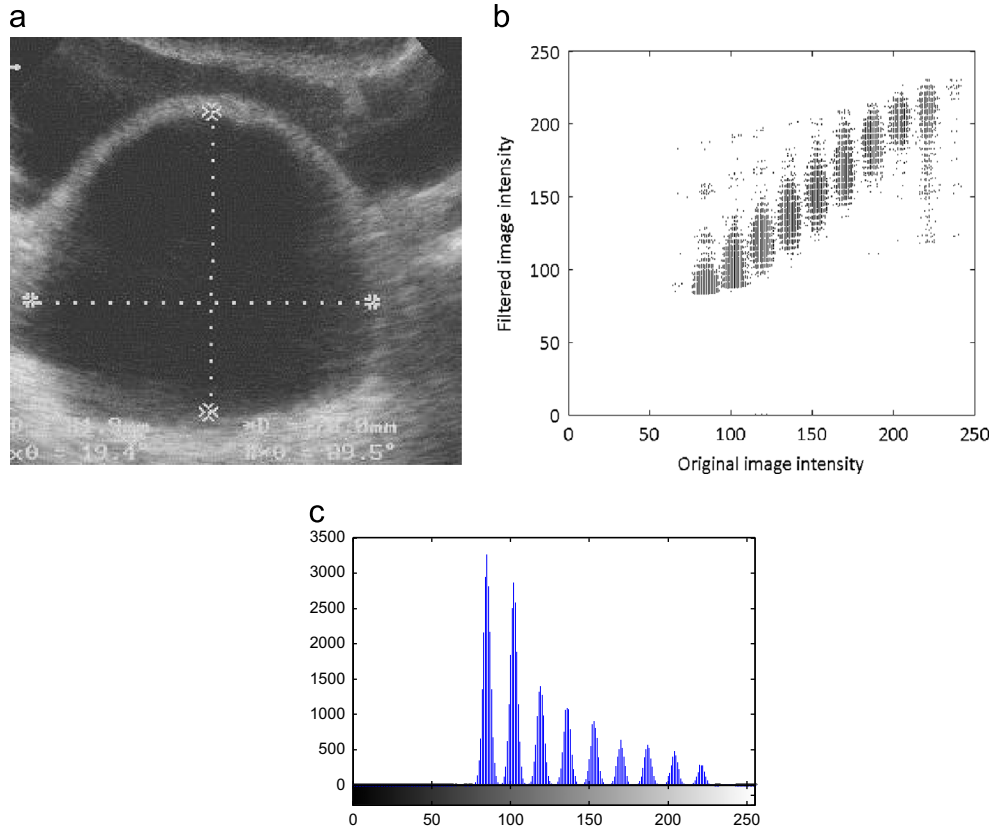


Fig. 3. (a) Original bladder image. (b) 2D input space, the horizontal axis is the original image intensity and the vertical axis is the intensity of filtered image. (c) Histogram of the bladder image.

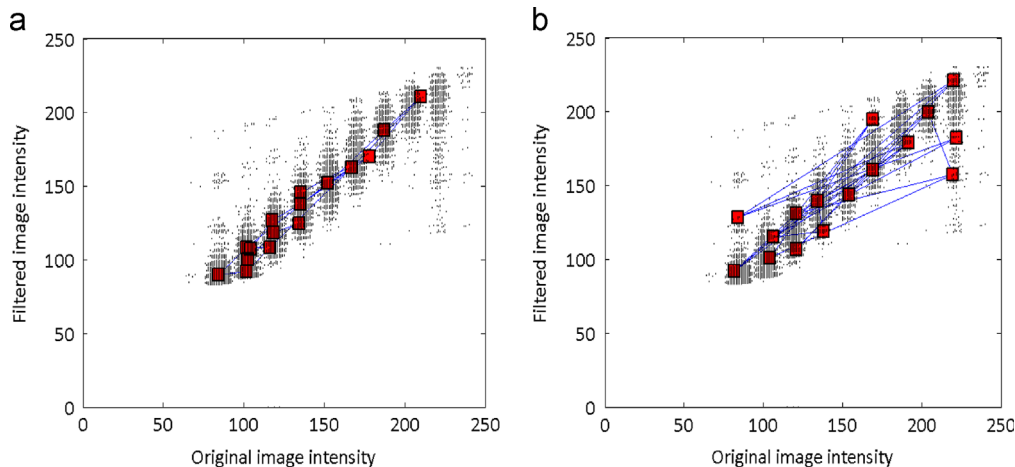


Fig. 4. Comparison of the SOM and MA-SOM networks: (a) structure of the MA-SOM network in the input space and (b) structure of the SOM network in the input space.

where η and λ are two parameters used to control the effects of the volume and the number of neurons of the cluster, respectively; and C is the number of clusters in the neurons' structure corresponding to t_i , and also D_{t_i} computes the density of clusters in the neurons' structure for each t_i .

After determining the best threshold value, its corresponding clusters are found by using (11)–(14). Then for each cluster, the objects in the segmented image, which belong to neurons of this cluster, are joined together. Therefore, after the merging process, a modified segmented image is formed.

3. Results

3.1. Comparison of SOM and MMA-SOM

In order to study the differences between SOM based method and the proposed method, we used both methods to segment an ultrasound (US) bladder image [24] as shown in Fig. 3(a). The SOM and MA-SOM networks had 4×4 structures in the first layer. The learning parameter μ and the effective width σ of both networks were equal to 0.05. In MA-SOM networks, the initial number of trace vectors was 5, and the values of Δt , η and λ were 1, 1 and 5, respectively. We utilized a 2D-DWT with a scale parameter 1 to create a filtered image. Intensities of the filtered and original images formed the 2D input space. Fig. 3(b) shows the distribution

of the input feature space. The horizontal and vertical axes denote the intensities of the original and filtered images respectively. Fig. 3(c) displays the histogram of the original image which shows that the intensities of pixels were mostly distributed around 85 and 110. This figure also indicates that when the intensity values increased, the densities of pixels decreased. After creating the 2D input space, 200 samples were randomly selected from it to build a training set. In order to train the SOM and the MA-SOM networks, we applied this training set 5 times to each network. In these networks, the weight vector of each neuron was updated by using update equations.

The structures of the trained SOM and MA-SOM are shown in Fig. 4(a) and (b), respectively. As Fig. 4(a) demonstrates, the proposed MA-SOM properly discovered the pattern of the input space. It is also evident in this figure that there was a direct relation between the image histogram and the MA-SOM result. More precisely, densities of neurons were high at the start, but they decreased with rise of intensity. However, as Fig. 4(b) shows, the SOM failed to know the input space. On the other hand, the sparse samples could not affect the structure of MA-SOM because of its filtering ability, however, they diverted the SOM from the input pattern. Fig. 5(a) shows the SOM result, and Fig. 5(b) and (c) illustrate the segmentation results of the MMA-SOM before and after the merging process, respectively. These figures show that a proper cluster identification led to a more accurate segmentation.

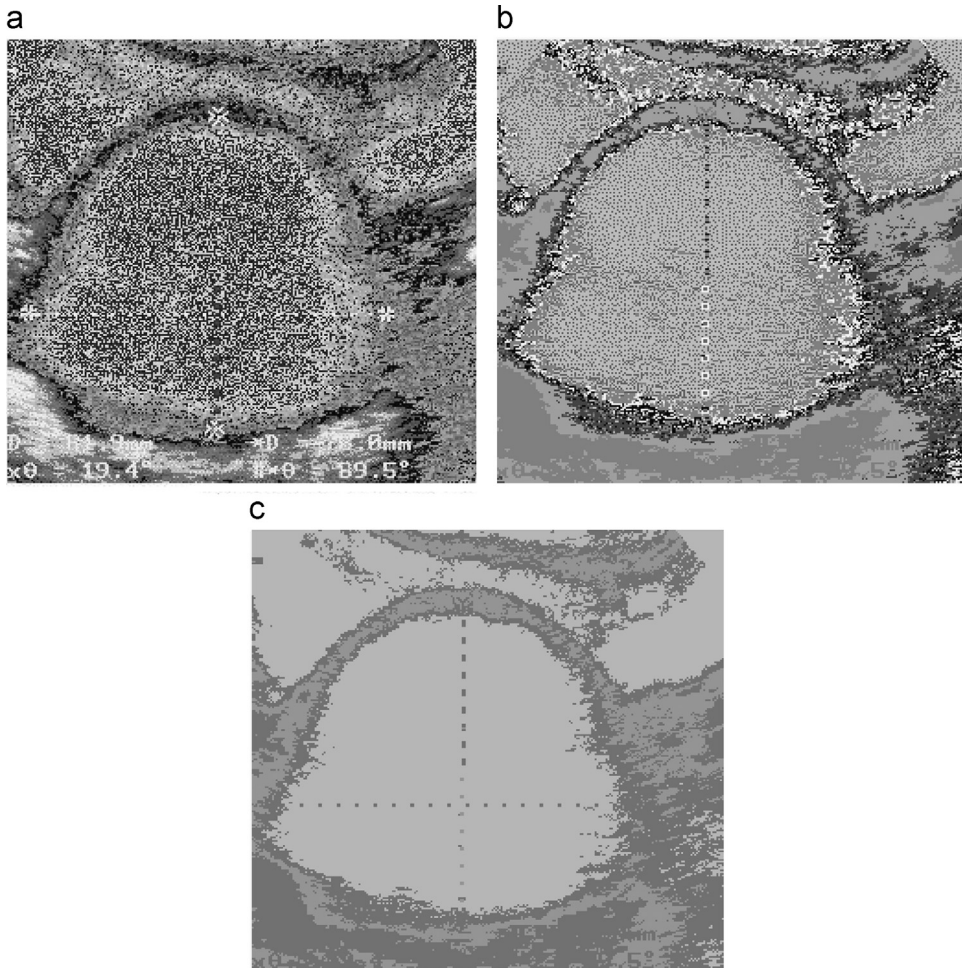


Fig. 5. Segmentation results of the bladder image: (a) segmentation result of the SOM network, (b) segmentation result of the proposed MMA-SOM method before merging process and (c) segmentation result of the proposed method after the merging process.

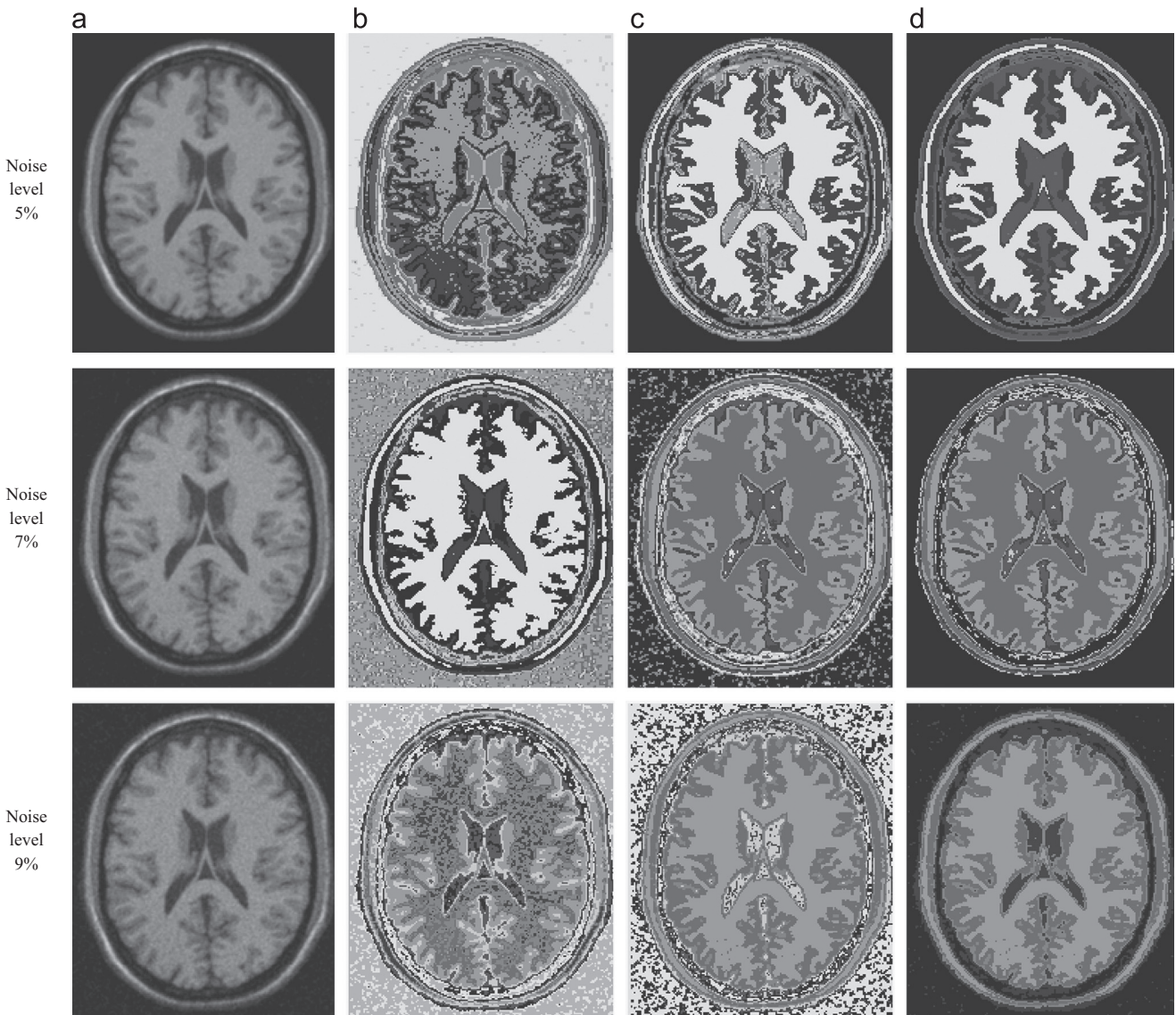


Fig. 6. Segmentation result of the MRI images with different noise levels: (a) original image, (b) segmentation result of the SOM network, (c) segmentation result of the proposed MMA-SOM method before merging process and (d) segmentation result of the proposed method after the merging process.

Table 1
Area error metrics for the white matter of the noisy MRI images.

Noise level (%)	TP	FP	SI
1	98.08	0.11	98.01
5	95.55	2.12	93.55
7	94.07	5.31	91.82
9	94.01	5.85	91.30

Table 3
Area error metrics for the CSF of the noisy MRI images.

Noise level (%)	TP	FP	SI
1	88.27	0.02	88.12
5	61.80	4.95	58.57
7	58.87	5.16	56.08
9	49.50	5.23	44.18

3.2. Noise field study

In order to evaluate the performance of the proposed algorithm in a noise field, we segmented 4 simulated normal brain images with 1%, 5%, 7% and 9% noise levels. The noise had Rayleigh statistics in the background and Rician statistics in the signal region. The noise percentage was representative of the standard deviation percent ratio of the white Gaussian noise versus the signal [26]. The noisy image, the segmentation result of the SOM, the segmentation result of the MMA-SOM before merging process and the

Table 2
Area error metrics for the gray matter of the noisy MRI images.

Noise level (%)	TP	FP	SI
1	98.01	0.04	98
5	90.89	5.11	85.59
7	89.98	5.69	86.29
9	88.76	5.41	81.94

segmentation result of the MMA-SOM after the merging process are shown in Fig. 6. As this figure shows, the accuracy of both SOM and MMA-SOM decreased as the noise level increased, but the MMA-SOM was more resistant to noise. Fig. 6(c) and (d) depict the

merging process effect. This effect can be clearly seen in the background part of the noisy images. For the evaluation of the MMA-SOM method, false positive (FP), true positive (TP) and similarity (SI) of the white matter, the gray matter and the CSF

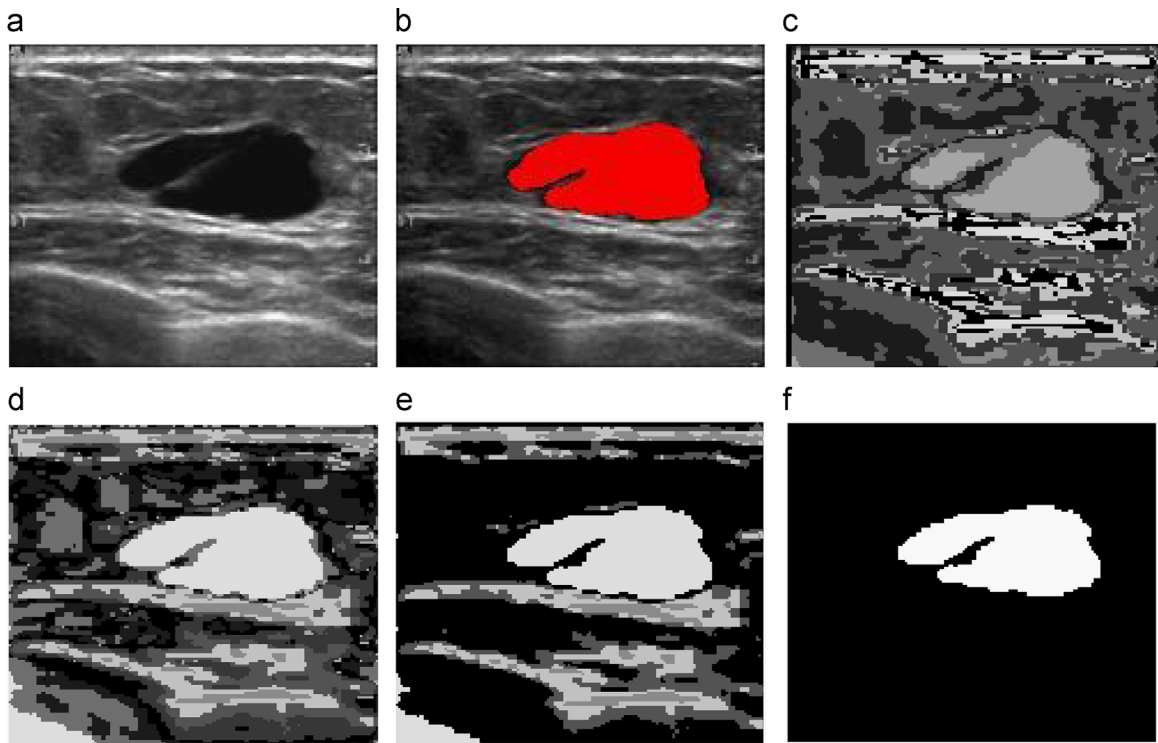


Fig. 7. Segmentation procedure of BUS images: (a) original images, (b) tumor region selected by the physician, (c) segmentation result of the SOM network, (d) segmentation result of the proposed MMA-SOM method before merging process, (e) segmentation result of the MMA-SOM method after merging process and (f) tumor region detected by the proposed method.

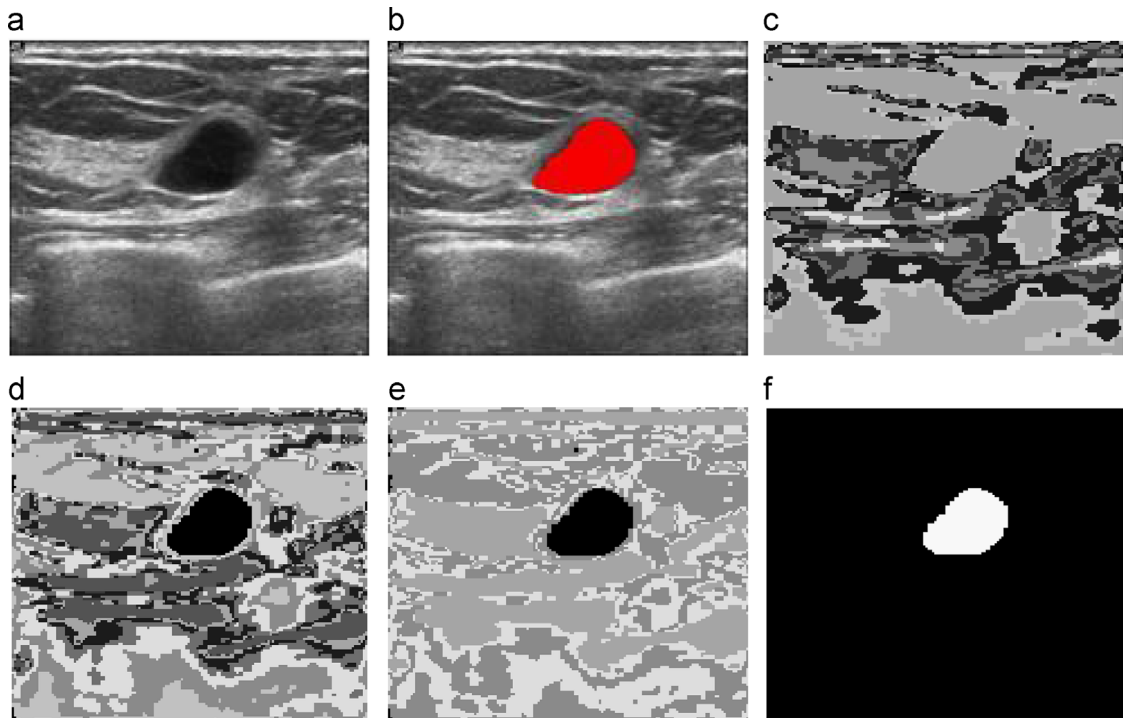


Fig. 8. Segmentation procedure of BUS images: (a) original images, (b) tumor region selected by the physician, (c) segmentation result of the SOM network, (d) segmentation result of the proposed MMA-SOM method before merging process, (e) segmentation result of the MMA-SOM method after merging process and (f) tumor region detected by the proposed method.

parts are shown in **Tables 1–3**, respectively. These tables demonstrate that for the white matter and the gray matter parts, MMA-SOM was resistant to noise but, for the CSF part, decrement in the segmentation accuracy was noticeable.

3.3. Segmentation of the medical images

In order to evaluate the proposed method, we used a dataset of 30 BUS images, 10 MRI head images [25] and one CT head image. The BUS images were collected by using a Siemens Antares ultrasound system. These images were obtained by the medical imaging center of the Imam Khomeini Hospital.

We segmented all medical images by using SOM and MA-SOM networks. The structures of both networks were 3×3 , the learning parameter μ and the effective width σ of both networks were equal to 0.05. The MA-SOM neurons had 5 trace vectors, and the values of T_0 , Z , Δt , η and λ were 20, 20, 1, 1 and 5, respectively. First we selected one of the images in the dataset as a training image. As we mentioned in **Section 2**, in the network training step, we asked a physician to determine the number of objects in the image; K . For threshold values from 0 to 255 and Δt , η and λ equal to 1, we segmented the training image using MA-SOM, then we applied the merging process to the output layer of the network. After the merging process, the minimum threshold value which resulted $K - 2$ neurons and maximum threshold value which leads to $K + 2$ neurons determined the values of T_0 and Z , respectively. These values defined a meaningful range for the threshold value. For the threshold values in this range, we asked the physician to evaluate the segmentation result of the MMA-SOM. If he (she) decided that more neurons should join (resp. disjoin), we increased (resp. decrease) the value of η and decreased (resp. increase) the value of λ . We repeated this process until the physician confirmed the segmentation result for the training image. These values could be different for other datasets. We utilized a 2D-DWT with scale parameters 1 and 2 to build two filtered images. The intensities of the filtered and original images formed the 3D input space. In order to train the network, we divided the original image into 20 separate sub-images and randomly selected 10 pixels out of each one. Then, we divided the 200 training samples into 2 subsets, each consisting of 100 samples. One set is used as the training set, and another one as the validation set. The network is trained by the training set 50 times, and its performance is validated by the validation set.

First, in order to prove the efficiency of the proposed MA-SOM network, we segmented BUS images using this method. Since BUS images had heavy speckle noise and low quality, segmenting them was a crucial task. Two examples of BUS images are shown in **Figs. 7** and **8(a)**, respectively. **Figs. 7** and **8(b)** illustrate the breast tumor indicated by an experienced physician. The segmentation results of the SOM network are shown in **Figs. 7** and **8(c)**, respectively. The segmentation results of the MMA-SOM method before and after the merging process are shown in **Figs. 7** and **8(d)**, respectively. The segmentation results of the proposed method after the merging process are shown in **Figs. 7** and **8(e)**, respectively.

In order to extract the tumor from the segmented images, we used the following algorithm introduced in [28]. First, we defined a center window: a window about one-half of the whole image size which was put at the image center. Second, if a region had no intersection with the center window and it was connected to the image boundaries, the region was deleted from the image. Finally, for the remaining regions, the following score formula was used to rank them.

$$R_n = \frac{\sqrt{Area}}{dis(C_n, C_0)var(C_n)}, \quad n = 1, \dots, k \quad (17)$$

where k was the number of regions; $Area$ was the number of pixels in the region; C_n was the center of the region; C_0 was the center of the image, and $var(C_n)$ was the variance of a small circular region centered at C_n (this circle was extracted from the original image). The final tumor region is shown in **Figs. 7** and **8(f)**. There were significant correlations between the tumor region selected by the physician and segmentation result of our proposed algorithm as **Figs. 7** and **8(f)** show.

There were some methods to evaluate the segmentation results [26,27]. In this study, we used the Jaccard index and the Rogers and Tanimoto's index to find the differences between the object obtained by our proposed method and the one selected by the physician. **Table 4** shows the evaluation results of our proposed method and those of the SOM network. The results of the proposed MMA-SOM method were much more suitable in all cases.

In order to analyze the differences between the tumor boundary detected by the proposed method and the tumor boundary determined by the physician, we used two boundary error metrics. The two error metrics are Hausdorff (HD) distance and mean absolute distance (MD) [23]. We showed the boundary detected by proposed method as $R = \{r_1, r_2, \dots, r_\alpha\}$ and the boundary manually delineated by the physician as $Q = \{q_1, q_2, \dots, q_\beta\}$. Each element of R or Q was a point on the corresponding contour. The shortest distance between any point of R (r_i) and all points of Q was defined as

$$d(r_i, Q) = \min ||r_i - q_j||, \quad i = 1, \dots, \alpha, \quad j = 1, \dots, \beta, \quad (18)$$

where α and β are the numbers of boundary pixels of contours R and Q , respectively, and $||\cdot||$ is 2D Euclidean distance.

HD and MD were defined as

$$HD = \max_i d(r_i, Q), \quad i = 1, \dots, \alpha \quad (19)$$

$$MD = \frac{\sum_{i=1}^{\alpha} d(r_i, Q)}{\alpha} \quad (20)$$

HD and MD computed the longest and the average distance between the two contours, respectively. The corresponding normalized errors Norm.HD and Norm.MD were computed by

$$\text{Norm.HD} = \frac{HD}{\beta}, \quad \text{Norm.MD} = \frac{MD}{\beta} \quad (21)$$

Tables 5–7 show the evaluation results of the proposed method and those of the SOM network. In all columns of these tables, the values of the boundary error metrics of the proposed method were lower than the SOM based method, which indicates the accuracy of the proposed MMA-SOM method.

Table 4
Mean of Jaccard index and Rogers and Tanimoto index for 30 BUS images.

Method	Jaccard index	Rogers Tanimoto index
SOM	51.64	46.22
MMA-SOM	86.80	86.88

Table 5
Boundary error metrics of the segmentation of the image in **Fig. 6(a)**.

Method	HD	MD
SOM	87.20	27.31
MMA-SOM	8.60	2.62

In order to test the performance of our proposed method, we used 10 anatomical models of the MRI head images from normal category of Brainweb site [25] in addition to the BUS images. These images were T1 with 1 mm slice thickness and the level of intensity non-uniformity (RF) was 20%. For these images, we

added a multiplicative noise to the original image (I), using the following equation:

$$J = I + (n \times I), \quad (22)$$

where n was a uniformly distributed random noise with the mean of 0 and the variance of 0.01, and j is the resulted noisy image. Fig. 9 shows the original image, segmentation result of the MA-SOM and the segmentation result of the MMA-SOM for 3 MRI images. Case 3 in this figure is a good example of the effect of the merging process. In the first look at Fig. 9(b) for case 3, it seems that MA-SOM network has failed to segment the image properly, but the accuracy of this network appears in Fig. 9(c) after joining the adjacent neurons. Table 8 shows the area error metrics for

Table 6
Boundary error metrics of the segmentation of the image in MEP_L_fig7Fig. 7 (a).

Method	HD	MD
SOM	87.77	2441
MMA-SOM	6.32	2.39

Table 7
Mean of boundary error metrics of the segmentation of 30 BUS images.

Method	HD	MD	HD.Norm	MD.Norm
SOM	57.32	31.56	1.05	0.769
MMA-SOM	7.54	2.34	0.0532	0.0185

Table 8
Mean of area error metrics for 10 anatomical models of MRI head images.

Tissue	TP	FP	SI
White matter	97.45	0.75	94.97
Gray matter	93.68	0.79	91.29
CSF	84.52	0.75	82.16

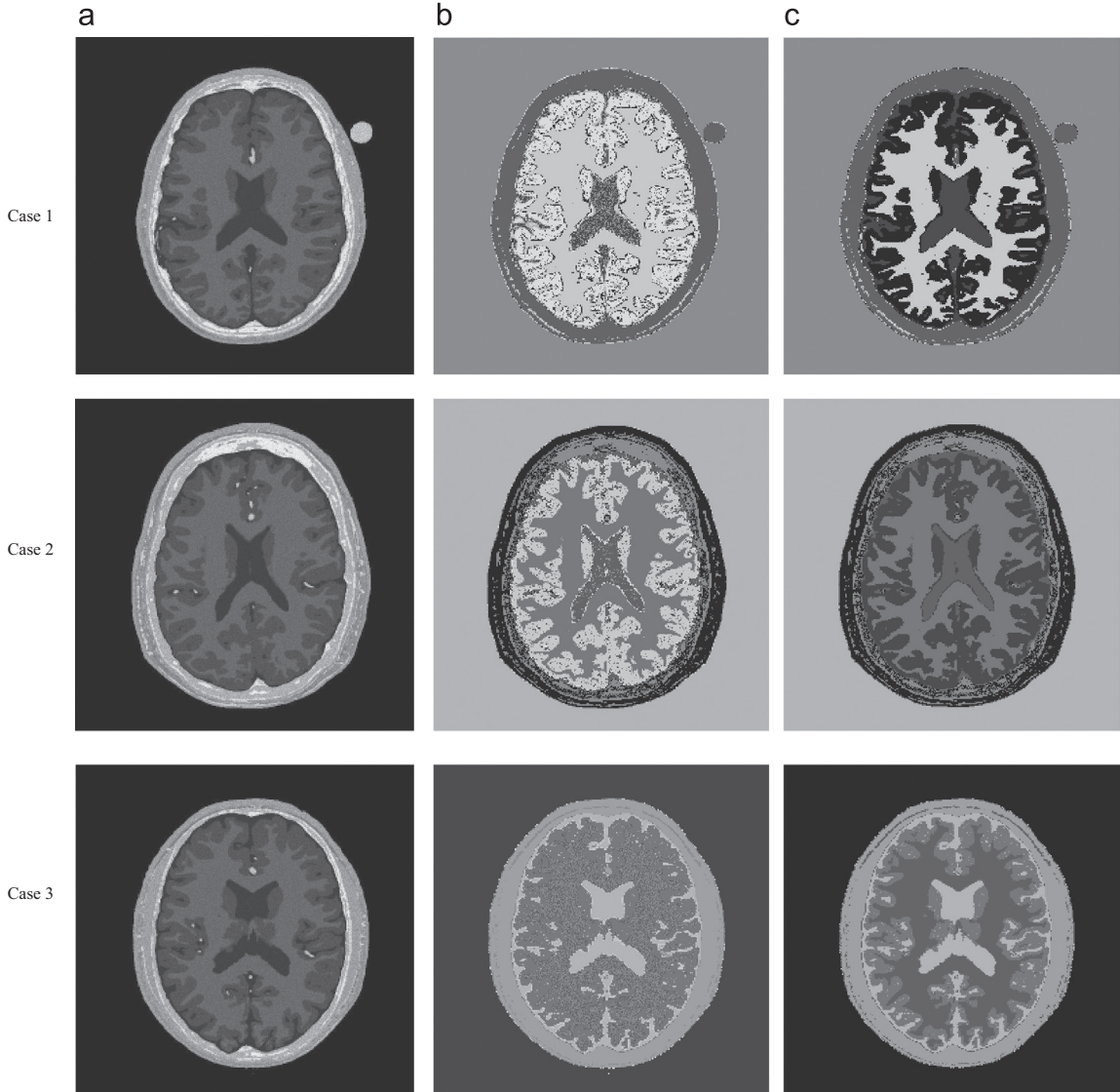


Fig. 9. Segmentation results of the MRI images using MMA-SOM: (a) original image, (b) segmentation result of the proposed MMA-SOM method before merging process and (c) segmentation result of the proposed method after the merging process.

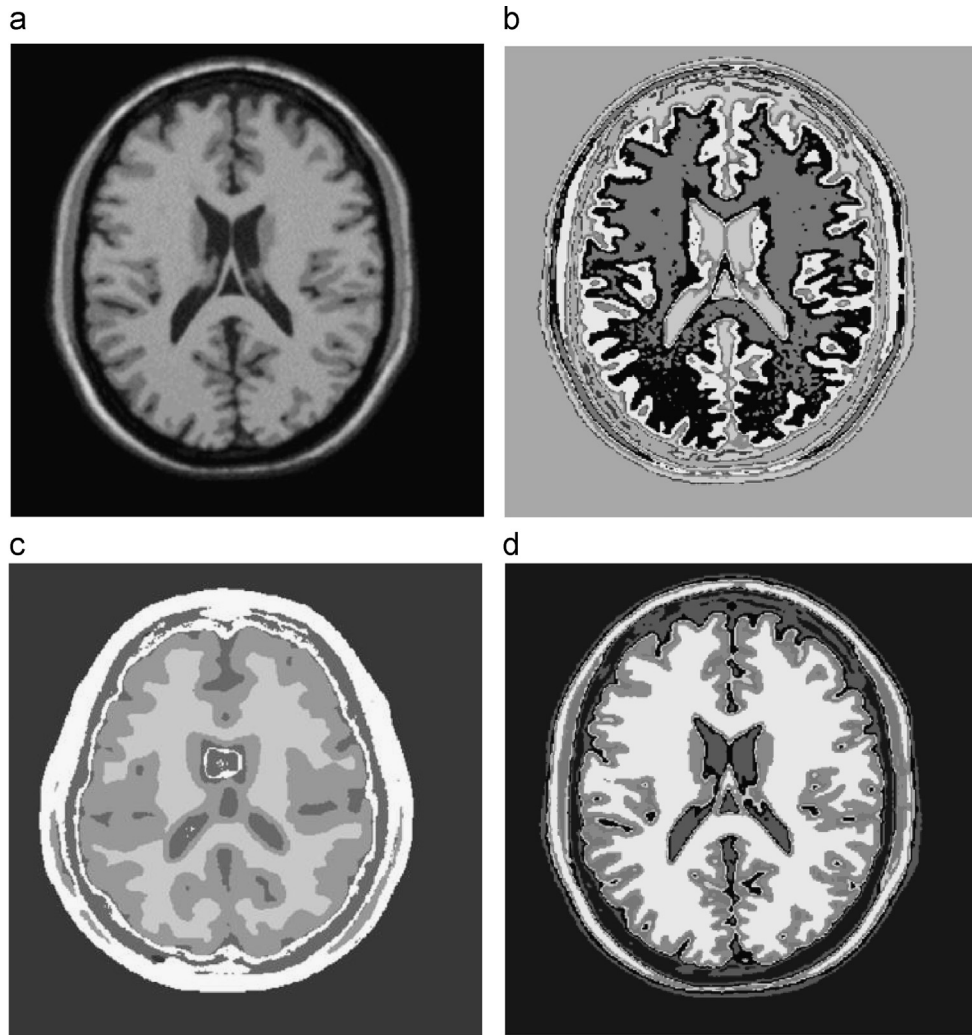


Fig. 10. Segmentation result of MRI head image: (a) original image, (b) segmentation result of the SOM network, (c) segmentation result of the ISNN method and (d) segmentation result of the proposed MMA-SOM method.

segmentation result of the gray matter, the white matter and the CSF parts, respectively. For all parts, the FP ratio was less than 0.8%, and the MMA-SOM segments of white and gray matter parts with TP ratio were more than 93%.

Finally, we segmented the CT and MRI images as shown in Figs. 10 and 11. Figs. 10 and 11(b) displays the segmentation results of the SOM network, and Figs. 10 and 11(c) show the segmentation results of the method in [20]. Figs. 10 and 11(d) display the segmentation results of the proposed MMA-SOM method. These figures depict the efficiency of the MMA-SOM segmenting method in comparison with that of the SOM network based method and the method in [20], and they also show the MMA-SOM method's capability to segment the medical images with different modalities.

4. Discussion

The main goal of this study is to show the benefits of merging MA-SOM network (MMA-SOM) for medical image segmentation by using default parameter sets (T_0 , Z , Δt , η and λ were 20, 20, 1, 1 and 5). The results which are presented in previous section are initial results since the number of datasets used, are not sufficient in order to draw any conclusions of statistical significance. Some of the defined parameters can play a critical role in the final outcome.

In this section, we study the effects of η and λ as the primary variables of MMA-SOM on the final result. It should be noted that the final result for different datasets could be improved if these parameters are set properly. Not only are former parameters used to control the effects of volume and number of neurons of cluster as mentioned before, but also they consequently can change the effect of the clusters density on a neuron's structure, and extracted objects. As shown in Fig. 12, a higher λ results in a higher threshold (T_{best}); the vice versa holds true for η . In addition, the mentioned parameters could be modified according to specific medical images. For example, while BUS images with more background noise need higher threshold and less λ subsequently, CT images with more accurate details need less T and higher λ (or less η). In the case of bladder image in Fig. 3(a), we computed the best threshold value, and the segmentation accuracy for different values of η and λ which are shown in Table 9. The segmentation result of this image with different threshold values is shown in Fig. 13. As this figure shows by means of changing threshold, user can focus on local or global objects.

5. Conclusions

In this paper, we proposed a new neural network based approach for medical image segmentation. In this method, we

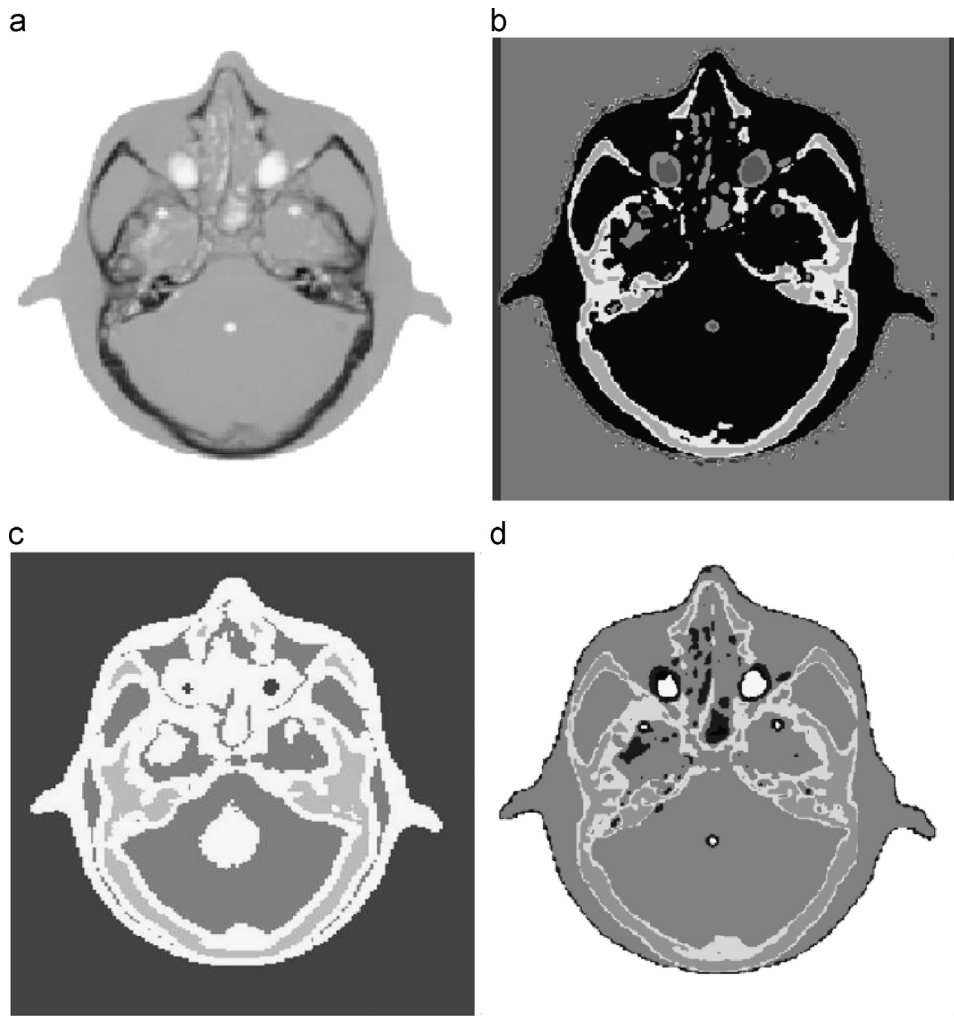


Fig. 11. Segmentation result of CT head image: (a) original image, (b) segmentation result of the SOM network, (c) segmentation result of the ISNN method and (d) segmentation result of the proposed MMA-SOM method.

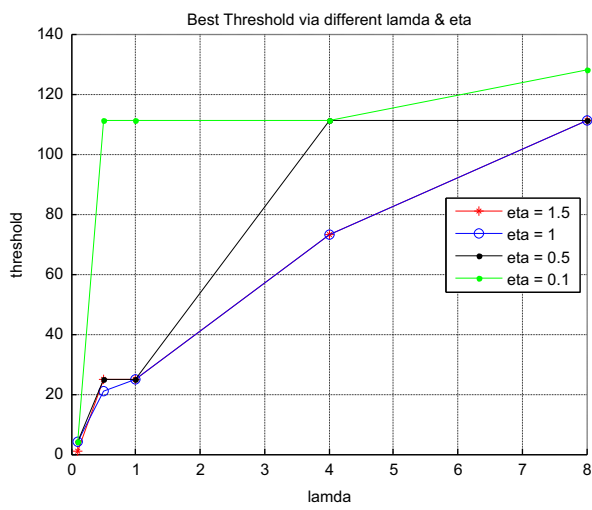


Fig. 12. Best threshold via different λ and η for bladder image in Fig. 3(a).

utilized a MA-SOM network for segmentation, and used its filtering ability to depress the image noise. After the image segmentation with the MA-SOM network, objects that belonged to a specific cluster were joined in a merging process.

Table 9

Evaluation of threshold and accuracy of MMA-SOM result via different η and λ values for Fig. 3(a).

λ	η	Best threshold	TP	FP
0.1	1	4	50.12	0.00
0.5	1	21	92.11	0.02
1	1	25	95.17	0.07
4	1	73	96.31	2.18
8	1	111	100.0	18.12
0.1	1.5	1	45.56	0.00
0.5	1.5	25	95.17	0.07
1	1.5	25	95.17	0.07
4	1.5	73	96.31	2.18
8	1.5	111	100.0	18.12
0.1	0.5	4	50.12	0.00
0.5	0.5	25	95.17	0.07
1	0.5	25	95.17	0.07
4	0.5	111	100.0	18.12
8	0.5	111	100.0	18.12
0.1	0.1	4	50.12	0.00
0.5	0.1	111	100.0	18.12
1	0.1	111	100.0	18.12
4	0.1	111	100.0	18.12
8	0.1	128	100.0	52.73

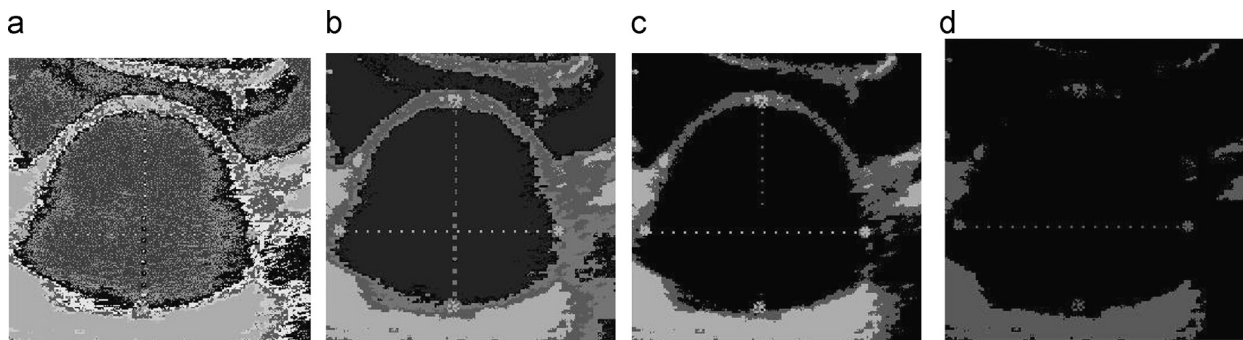


Fig. 13. Segmentation results of Fig. 3(a) with three different thresholds: (a) $T_{best}=4$, (b) $T_{best}=25$, (c) $T_{best}=111$, and (d) $T_{best}=128$.

The experimental results showed that MMA-SOM was robust to noise and it determined the input image pattern properly. In the noise field study section, we analyzed the noise level impact on the performance of the MMA-SOM and the SOM methods in 4 MRI images with different noise levels. In all cases, the MMA-SOM showed a better performance in comparison with the SOM. MMA-SOM could depress the noise effect for the white and gray matter parts, but decrement of its performance was noticeable for the CSF part. We used 30 BUS images to evaluate the performance of our proposed method. The results showed that there were significant correlations between the tumor region segmented by our proposed method and the one selected by a physician. The Jaccard index together with the Rogers and Tanimoto index confirm the accuracy of our proposed method in comparison with that of the SOM network based method. We studied the performance of our proposed method with the other 10 noisy MRI images. The FP ratio less than 0.8% for all parts and TP ratio more than 93% for the white matter and the gray matter parts demonstrate the accuracy of the MMA-SOM method. The presented method also segmented CT and MRI head images much better than the ISNN and SOM network based methods.

In our future works, we aim to fully automate our proposed segmenting method and integrate it into CAD systems.

Conflict of interest statement

None declared.

References

- [1] R.C. Gonzalez, R.E. Woods, *Digital Image Processing*, Addison-Wesley, Reading, MA, 1992.
- [2] J. Canny, A computational approach to edge detection, *IEEE Trans. Pattern Anal. Mach. Intell.* 8 (1986) 679–698.
- [3] J.R. Parker, *Algorithms for Image Processing and Computer Vision*, Wiley New York, 1997.
- [4] L. Lemieux, G. Hagemann, K. Krakow, F.G. Woermann, Fast, accurate, and reproducible automatic segmentation of the brain in T1 weighted volume MRI data, *Magn. Reson. Med.* 42 (1999) 127–135.
- [5] R. Pohle, K.D. Toennies, Segmentation of medical images using adaptive region growing, *Proc. SPIE-Med. Imaging* 4322 (2001) 1337–1346.
- [6] T.Y. Law, P.A. Heng, Automated extraction of bronchus from 3D CT images of lung based on genetic algorithm and 3D region growing, *Proc. SPIE-Med. Imaging* 3979 (2000) 906–916.
- [7] S.R. Kannan, A new segmentation system for brain MR images based on fuzzy techniques, *J. Appl. Soft Comput.* 8 (2008) 1599–1606.
- [8] K.S. Chuang, et al., Fuzzy c -means clustering with spatial information for image segmentation, *Comput. Med. Imaging Graph.* 30 (2006) 9–15.
- [9] K.S. Al-Sultan, C.A. Fedjki, A Tabu search-based algorithm for the fuzzy clustering problem, *Pattern Recognition* 30 (1997) 2023–2030.
- [10] M.N. Ahmed, et al., Modified fuzzy C-means algorithm for bias field estimation and segmentation of MRI data, *IEEE Trans. Med. Imaging* 21 (2002) 193–199.
- [11] J. Noble, D. Boukerroui, Ultrasound image segmentation: a survey, *IEEE Trans. Med. Imaging* 25 (2006) 987–1010.
- [12] J. Jiang, P. Trundle, J. Ren, Medical image analysis with artificial neural networks, *Comput. Med. Imaging Graph.* 34 (2010) 617–631.
- [13] S. Powell, V.A. Magnotta, H. Johnson, V.K. Jammalamadaka, R. Pierson, N.C. Andreasen, Registration and machine learning-based automated segmentation of subcortical and cerebellar brain structures, *NeuroImage* 39 (2008) 238–247.
- [14] P.L. Chang, W.G. Teng, Exploiting the self-organizing map for medical image segmentation, in: 20th IEEE International Symposium on Computer-Based Medical Systems, vol. 7, 2007, pp. 281–288.
- [15] Z. Iscan, M.N. Kurnaz, Z. Dokur, T. Olmez, Ultrasound image segmentation by using wavelet transform and self-organizing neural network, *Neural Inform. Process.—Lett. Rev.* 10 (8–9) (2006) 183–191.
- [16] C.Y. Chang, P.C. Chung, Medical image segmentation using a contextual constraint-based Hopfield neural cube, *Image Vision Comput.* 19 (2001) 669–678.
- [17] K.S. Cheng, J.S. Lin, C.W. Mao, Application of competitive Hopfield neural network to medical image segmentation, *IEEE Trans. Med. Imaging* 15 (1996) 560–561.
- [18] Z. Xiao, J. Shi, Q. Chang, Automatic image segmentation algorithm based on PCNN and fuzzy mutual information, in: IEEE International Conference on Computer and Information Technology, 2009, pp. 241–245.
- [19] T. Kohonen, *Self-organization, and Associative Memory*, Springer-Verlag, Berlin, 1989.
- [20] Z. Iscan, A. Yuksel, Z. Dokur, M. Korurek, T. Olmez, Medical image segmentation with transform and moment based features and incremental supervised neural network, *Digital Signal Process.* 19 (2009) 890–901.
- [21] M. Tucci, M. Raugi, Adaptive FIR neural model for centroid learning in self-organizing maps, *IEEE Trans. Neural Networks* 21 (2010).
- [22] S. Haykin, *Neural Networks: A Comprehensive Foundation*, 2nd ed., Prentice-Hall, 1999.
- [23] A. Madabhushi, D.N. Metaxas, Combining low-, high-level and empirical domain knowledge for automated segmentation of ultrasonic breast lesions, *IEEE Trans. Med. Imaging* 22 (2) (2003) 155–169.
- [24] (http://www.drgdiaz.com/ascitis_bladder.shtml).
- [25] (<http://www.bic.mni.mcgill.ca/brainweb/>).
- [26] J.K. Udupa, V.R. LeBlanc, Z.G. Ying, C. Imielinska, H. Schmidt, L.M. Currie, B.E. Hirsch, J. Woodburn, A framework for evaluating image segmentation algorithms, *Comput. Med. Imaging Graph.* 30 (2) (2006) 75–87.
- [27] W.R. Crum, O. Camara, D.L.G. Hill, Generalized overlap measures for evaluation and validation in medical image analysis, *IEEE Trans. Med. Imaging* 25 (11) (2006) 1451–1461.
- [28] J. Shan, H.D. Cheng, Y. Wang, A novel automatic seed point selection algorithm for breast ultrasound images, in: 19th International Conference on Pattern Recognition, 2008, pp. 1–4.
- [29] A. Hassanien, H. Al-Qaheri, E.A. El-Dahshan, prostate boundary detection in ultrasound images using biologically-inspired spiking neural network, *Appl. Soft Comput.* 11 (2) (2011) 2035–2041.
- [30] A. Hassanien, T. Kim, Breast cancer MRI diagnosis approach using support vector machine and pulse coupled neural network, *J. Appl. Logic* 10 (4) (2012) 277–284.